J. Fluid Mech. (1991), *vol.* 225, *pp.* 655–671
Printed in Great Britain

Steady incompressible flow past a row of circular cylinders

By BENGT FORNBERG
Corporate Research, Exxon Research and Engineering Company, Annandale, NJ 08801, USA

(Received 30 July 1990)

Numerical solutions are presented for steady two-dimensional incompressible flow past an infinite row of cylinders (of unit radii, with distances W between their centres). The calculations cover $R \leqslant 700$ for $5 \leqslant W \leqslant \infty$ and also $R = 800$ for $5 \leqslant W \leqslant 100$ (where R denotes the Reynolds number based on the cylinder diameters). The recirculation regions (wake bubbles) are found to grow in length approximately linearly with R in all cases. For high values of R, a major change occurs in their character when W is increased past $W_{\text{crit}} \approx 16$. While they have remained slender up to this point (essentially only stretching in length in proportion to R), their centres of circulation have moved towards their ends. As W is further increased, the wake bubbles widen rapidly, beginning from the rear of the wakes. In the limit of $W \to \infty$, the present results agree with the previous ones for a single cylinder as reported by Fornberg (1985).

1. Introduction

The arrangement of cylinders considered in this study is illustrated in figure 1; symmetry is assumed in the flow fields about the dashed horizontal lines. Previous results for steady flows in this (or similar) geometries are summarized, for example, in the introduction of Ingham, Tang & Morton (1990). In particular, results by Smith (1985) and by Milos & Acrivos (1986) indicate that, for small cylinder separations W, the lengths of the recirculation regions will grow indefinitely with R (the Reynolds number). However, these solutions (which can be obtained from boundary-layer approximations) fail to exist above a certain W_{crit}. By numerical solution of the Navier–Stokes equations for still higher values of W (in the similar context of an expanding channel with slip walls), Milos, Acrivos & Kim (1987) found two other, qualitatively distinct regimes. The first one (for W just above W_{crit}) again featured growing wakes. For even larger W, finite-sized Prandtl–Batchelor wakes were obtained (Batchelor 1956).

The present study confirms the first two of these three regimes and details the transition between them, but finds no evidence for the third regime (cf. some comments at the end of §7). In the limit of $W \to \infty$, the present solutions tend smoothly towards the ones previously reported for a single cylinder (Fornberg 1985).

Two separate codes were developed in order to effectively cover the cases of both 'narrow' ($W \leqslant 40$) and 'wide' ($W \geqslant 40$) cylinder separations (in the following denoted 'narrow code' and 'wide code' respectively). In both cases, the numerical approach consisted in approximating the governing equations by second-order centred finite differences on conformally mapped and stretched grids. The resulting algebraic systems were then solved by (quadratically convergent) Newton iterations.

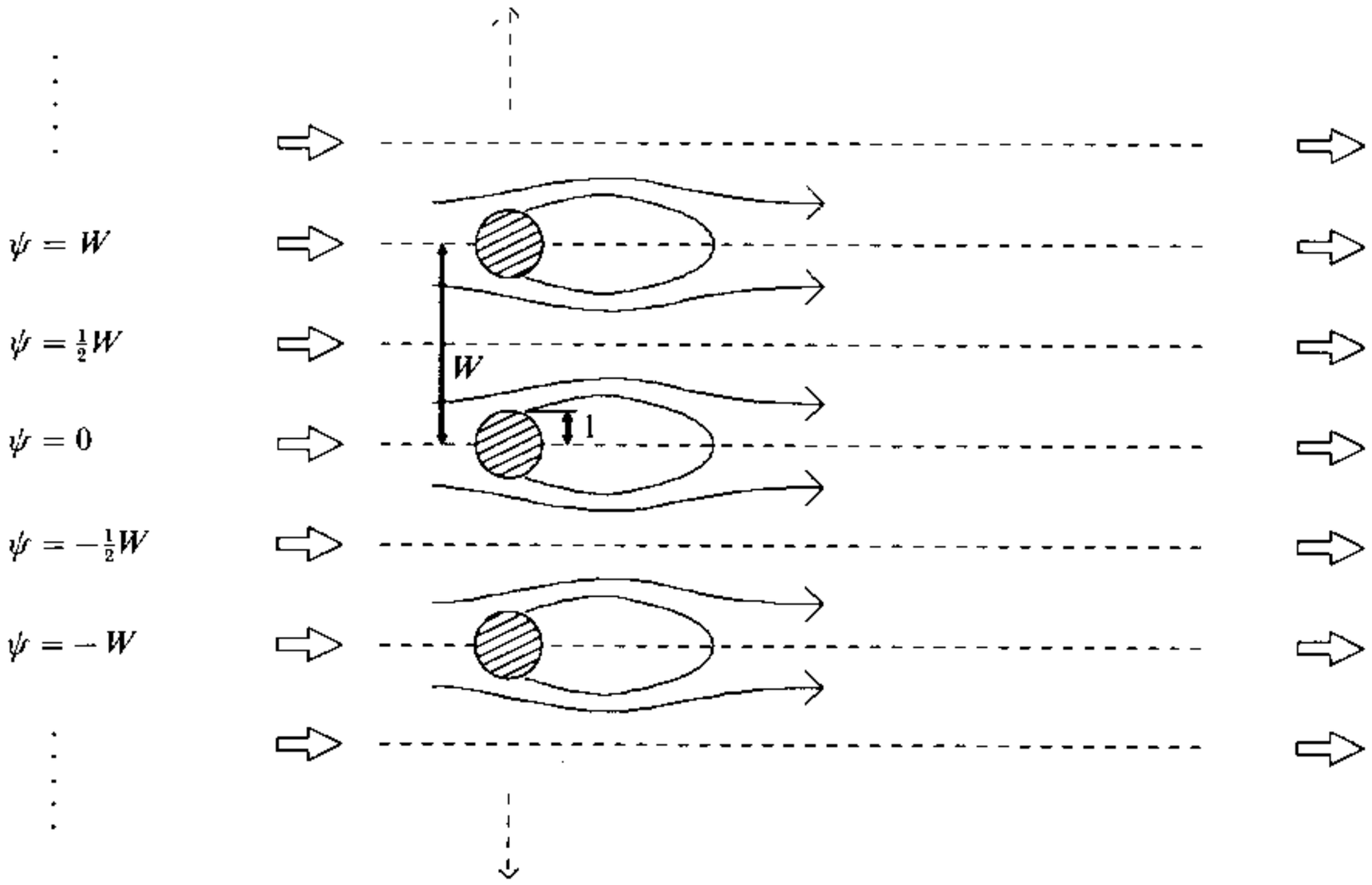

FIGURE 1. Schematic of flow configuration.

2. Mathematical formulation

In stream function–vorticity formulation (cylinders of radii 1 and Reynolds number R based on the cylinder diameters), the steady Navier–Stokes equations take the form

$$\frac{\partial^2 \Psi}{\partial x^2} + \frac{\partial^2 \Psi}{\partial y^2} + \omega = 0, \tag{1}$$

$$\frac{\partial^2 \omega}{\partial x^2} + \frac{\partial^2 \omega}{\partial y^2} + \tfrac{1}{2}R\left\{\frac{\partial \Psi}{\partial x}\frac{\partial \omega}{\partial y} - \frac{\partial \Psi}{\partial y}\frac{\partial \omega}{\partial x}\right\} = 0. \tag{2}$$

The two boundary conditions on the body surface are $\Psi = \partial\Psi/\partial n = 0$. On the two primary symmetry lines $y = 0$ and $y = \frac{1}{2}W$ (cf. figure 1), the conditions are $\Psi = \omega = 0$ and $\Psi = \frac{1}{2}W$, $\omega = 0$ respectively. Finally, $\Psi = y$ and $\omega = 0$ hold as $x \to \pm\infty$ ('free stream').

3. Generation of computational grids

An arbitrary conformal mapping from a complex $(X = x + \mathrm{i}y)$-plane to a $(Z = \xi + \mathrm{i}\eta)$-plane introduces only one additional factor in one of the governing equations. After such a mapping, (1) and (2) become

$$\left\{\frac{\partial^2 \Psi}{\partial \xi^2} + \frac{\partial^2 \Psi}{\partial \eta^2}\right\}\left|\frac{dZ}{dX}\right|^2 + \omega = 0, \tag{3}$$

$$\frac{\partial^2 \omega}{\partial \xi^2} + \frac{\partial^2 \omega}{\partial \eta^2} + \tfrac{1}{2}R\left\{\frac{\partial \Psi}{\partial \xi}\frac{\partial \omega}{\partial \eta} - \frac{\partial \Psi}{\partial \eta}\frac{\partial \omega}{\partial \xi}\right\} = 0. \tag{4}$$

	$W\to\infty$	$W=100$	$W=50$	$W=20$	$W=10$	$W=5$
V	$>W$	99.96710348	49.93421993	19.83577431	9.67308621	4.35640639
α_1	1	1.00032910	1.00131768	1.00829321	1.03404008	1.15317637
α_2	0	−0.00000002	−0.00000035	−0.00001364	−0.00022418	−0.00409423
α_3	0			0.00000003	0.00000211	0.00015600
α_4	0				−0.00000002	−0.00000624
α_5	0					0.00000025
α_6	0					−0.00000001

TABLE 1. Values of the parameters V and $\{\alpha_i\}$ for some values of W

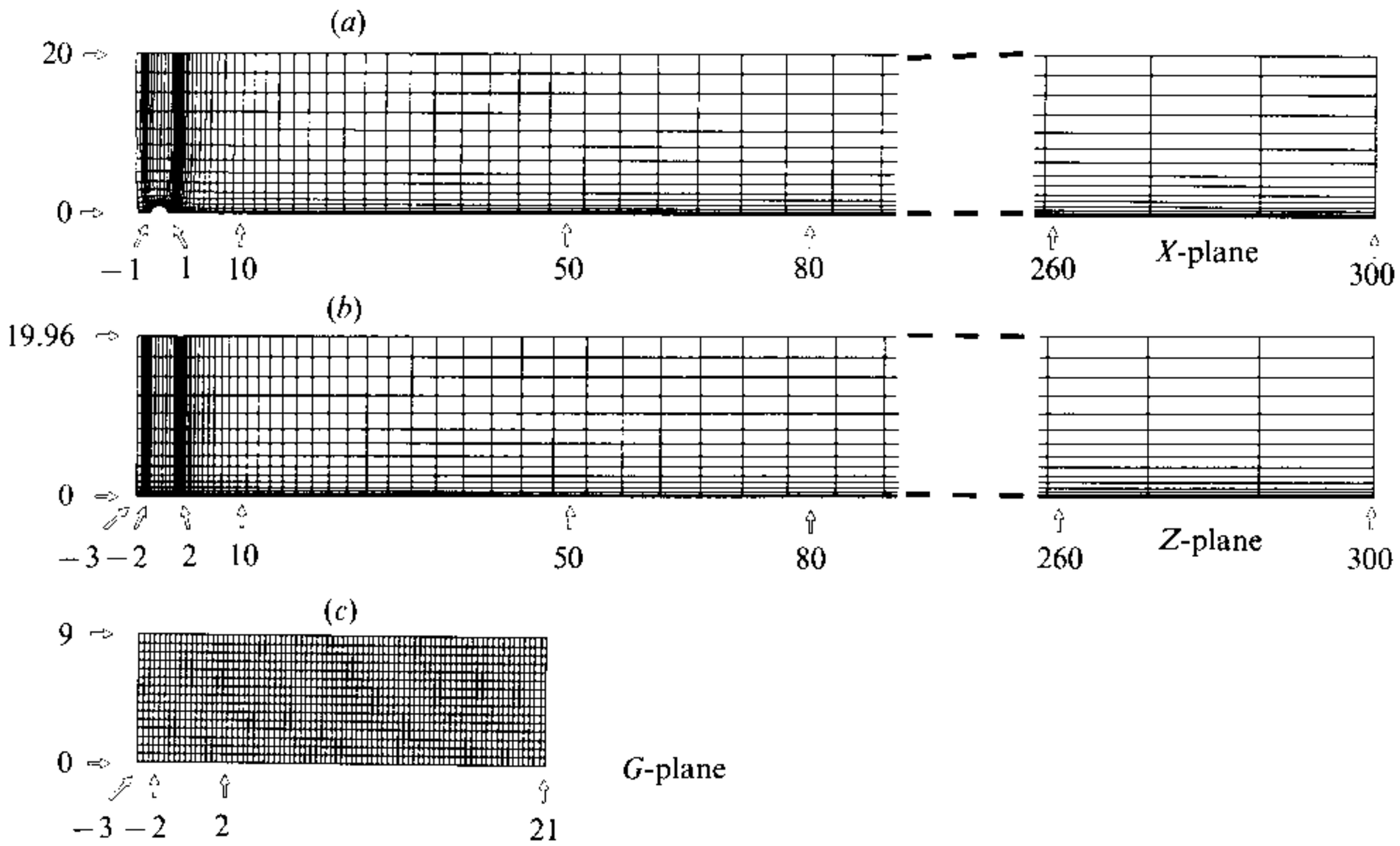

FIGURE 2. Examples of grids used in the 'narrow code', shown here for $W=40$, $M=79$ and $N=16$ (corresponding to $M=937$, $N=181$ with one out of every 12 grid lines displayed).

3.1. *Narrow code* ($W\leqslant 40$)

In this case, we want first to find a convenient representation of the conformal mapping $X=X(Z)$ between the flow domain $0\leqslant \operatorname{Im} X\leqslant \frac{1}{2}W$ minus the unit circle $|X|=1$ in the X-plane and an infinite strip in the Z-plane. This can be achieved by eliminating T between the expressions

$$Z=\frac{V}{W}\{X+\alpha_1 T+\alpha_2 T^3+\alpha_3 T^5+\ldots\}, \tag{5}$$

and

$$T=\frac{\pi}{W}\coth\left(\frac{\pi}{W}X\right). \tag{6}$$

For any real values of the parameters V and $\{\alpha_i\}$, equations (5) and (6) map $\operatorname{Im} X=0$ to $\operatorname{Im} Z=0$ and $\operatorname{Im} X=\frac{1}{2}W$ to $\operatorname{Im} Z=\frac{1}{2}V$. We want to find values for these parameters such that the unit circle $|X|=1$ also maps to a section of the real Z-axis, for example $-2\leqslant Z\leqslant 2$. To achieve this, one can consider the Laurent expansion (in powers of X) of the right-hand side of (5) (in the present calculations obtained by

τ	-3	-2	2	21	σ	0	9
ξ	-3	-2	2	300	η	0	19.96
$\partial\xi/\partial\tau$		0.3	0.3		$\partial\eta/\partial\sigma$	0.2	
$\partial^2\xi/\partial\tau^2$		0	0		$\partial^2\eta/\partial\sigma^2$	0	0
	↑	↑	↑	↑		↑	↑
$\xi(\tau) =$		cubic	quintic	cubic	$\eta(\sigma) =$		quartic
		$(W \leqslant 40)$					$(W = 40)$

TABLE 2. Parameters for grid stretching, narrow code ($Z = \xi + \mathrm{i}\eta$, $G = \tau + \mathrm{i}\sigma$)

numerical Taylor expansion of odd powers of $X \coth X$, by the method described by Fornberg 1981*a*, *b*). Requiring that, for each $k = 1, 3, 5, \ldots$, the X^k and X^{-k} terms in this expansion of (5) have equal (real) coefficients, thus causing the unit circle $|X| = 1$ to map to the real axis, leads, in a straightforward manner, to a rapidly converging iteration process for determining V and $\{\alpha_i\}$. Table 1 gives values for V and $\{\alpha_i\}$ corresponding to some choices of W. The series in (5) is seen to converge very rapidly.

The mapping just described takes a region in the X-plane, as shown in figure 2(*a*), and transforms it to a rectangle in the Z-plane (figure 2*b*). Since the resolution requirements are different in different parts of this rectangle, we consider a further plane (G-plane, figure 2*c*). We use an equispaced grid in this plane; the mapping between the Z- and the G-planes consists of independent grid stretchings in the two space directions: vertically a quartic polynomial with inflexion points at the two edges, horizontally a cubic–quintic–cubic spline with nodes (which are also inflexion and fix points) at -2 and 2. The additional free parameters (cf. table 2) were chosen to give enhanced resolution in the boundary layer and at the front and back stagnation points on the cylinder, to compensate for singularities in the conformal mapping at these points.

Figure 2(*a*–*c*) shows the grids used for $W = 40$, although only every 12th grid line is marked (horizontally and vertically; actual grids up to 937×181 were used *vs.* 79×16 shown in figure 2).

3.2. *Wide code* ($W \geqslant 40$)

Even with use of vertical grid stretching, it turns out to be computationally very uneconomical to use grids which extend all the way between $\mathrm{Im}\, X = 0$ and $\mathrm{Im}\, X = \frac{1}{2}W$ if W is large. Therefore, for $W \geqslant 40$, we instead use a grid which is just wide enough to enclose the area where ω is non-zero. The required vertical periodicity is implemented by a suitable boundary condition along the top edge of this computational domain. A convenient mapping $X = X(Z)$ for this case can again be expressed by means of an auxiliary variable T:

$$T = \alpha Z + \frac{5}{2}\left\{\arctan\frac{7Z+40}{15} + \arctan\frac{7Z-40}{15}\right\}, \tag{7}$$

and

$$T = X^{\frac{1}{2}} + X^{-\frac{1}{2}}. \tag{8}$$

For any value of α, $X < -1$ maps to the positive imaginary axis $-\mathrm{i}Z > 0$. With the choice

$$\alpha = 1 - \tfrac{5}{4}\{\arctan\tfrac{54}{15} - \arctan\tfrac{26}{15}\} \approx 0.685\ldots \tag{9}$$

the unit circle $|X| = 1$ maps to $0 \leqslant Z \leqslant 2$ and $X > 1$ to $Z > 2$.

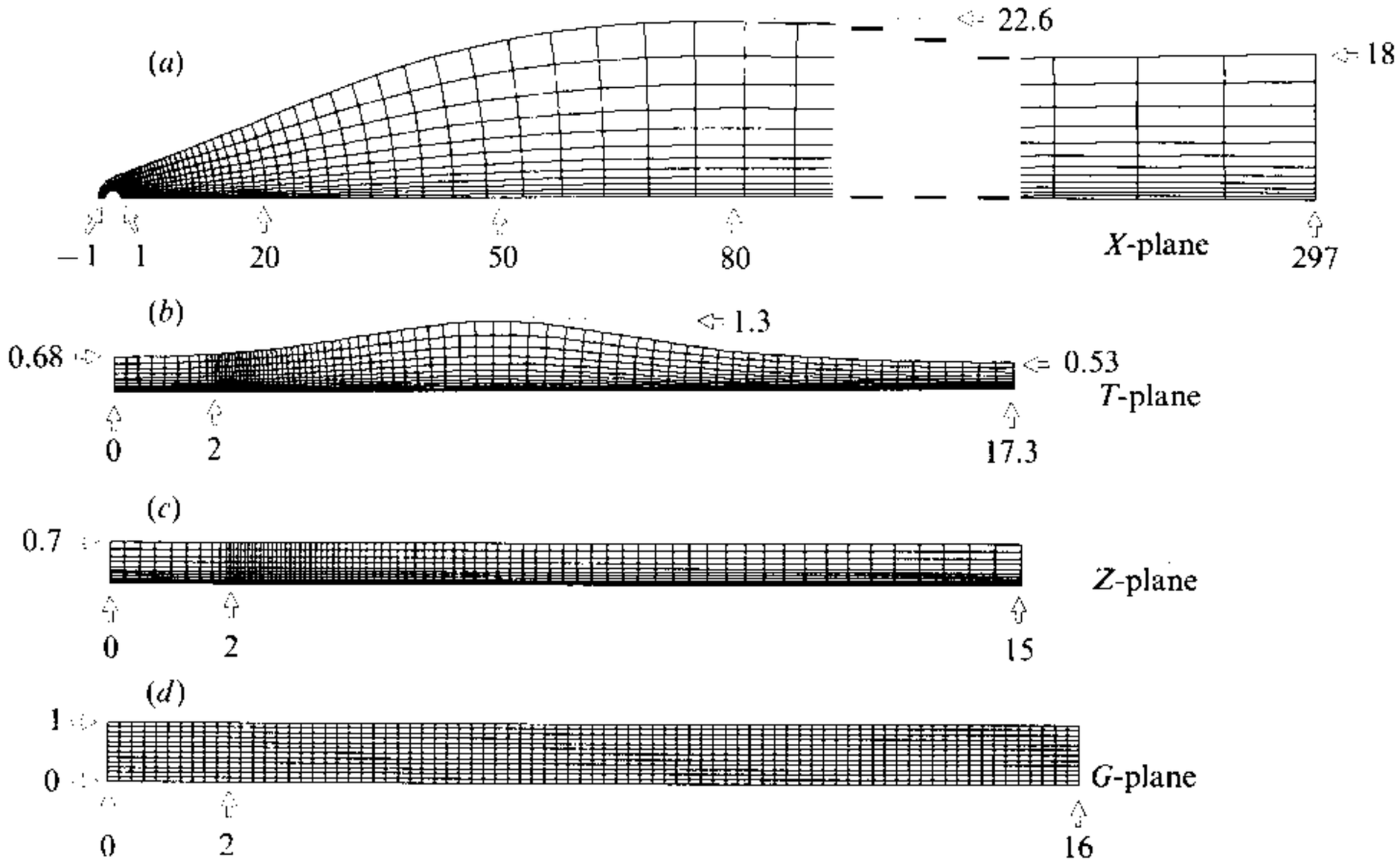

FIGURE 3. Examples of grids used in the 'wide code', shown here for $M = 81$ and $N = 13$. Actual grid densities ranged up to $M = 701$, $N = 121$.

τ	0	2	16	σ	0	1	
ξ	0	2	15	η	0	0.7	
$\partial\xi/\partial\tau$	0.7	0.1		$\partial\eta/\partial\sigma$	0.2		
$\partial^2\xi/\partial\tau^2$	0	0		$\partial^2\eta/\partial\sigma^2$	0		
	↑	↑	↑		↑	↑	
$\xi(\tau) =$		quintic	cubic	$\eta(\sigma) =$		cubic	

TABLE 3. Parameters for grid stretching, wide code ($Z = \xi + i\eta$, $G = \tau + i\sigma$)

Figure 3(*a–c*) shows how these mappings bring a physically suitable domain to rectangular shape. As in the case of the narrow code, a last mapping uses a G-plane with an equispaced grid (figure 3*d*). To get from the G-plane to the Z-plane, we use a cubic polynomial vertically (with inflexion point at the bottom edge) and a quintic–cubic spline horizontally with nodes (also inflexion and fix points) at 0 and 2 (cf. table 3). Figure 3(*a–d*) shows grids with about 1/10th of the maximal density used (up to 701×121 *vs.* 81×13 displayed here).

4. Numerical method

The numerical methods used in this study follow very closely the ones previously employed in Fornberg (1985, 1988). Therefore, the description here is brief and focuses mainly on the differences to the previous implementations.

The governing equations are approximated by centred, second-order finite differences. Potential flow is subtracted from Ψ before (3) and (4) are discretized. For the narrow code, this amounts simply to subtracting $\Psi_{\text{pot}} = (W/V)\,\text{Im}\,Z$. For the wide code, finding Ψ_{pot} (and its derivatives with respect to ξ and η) requires transformations from the Z-plane of equations (7) and (8) to the X-plane and then

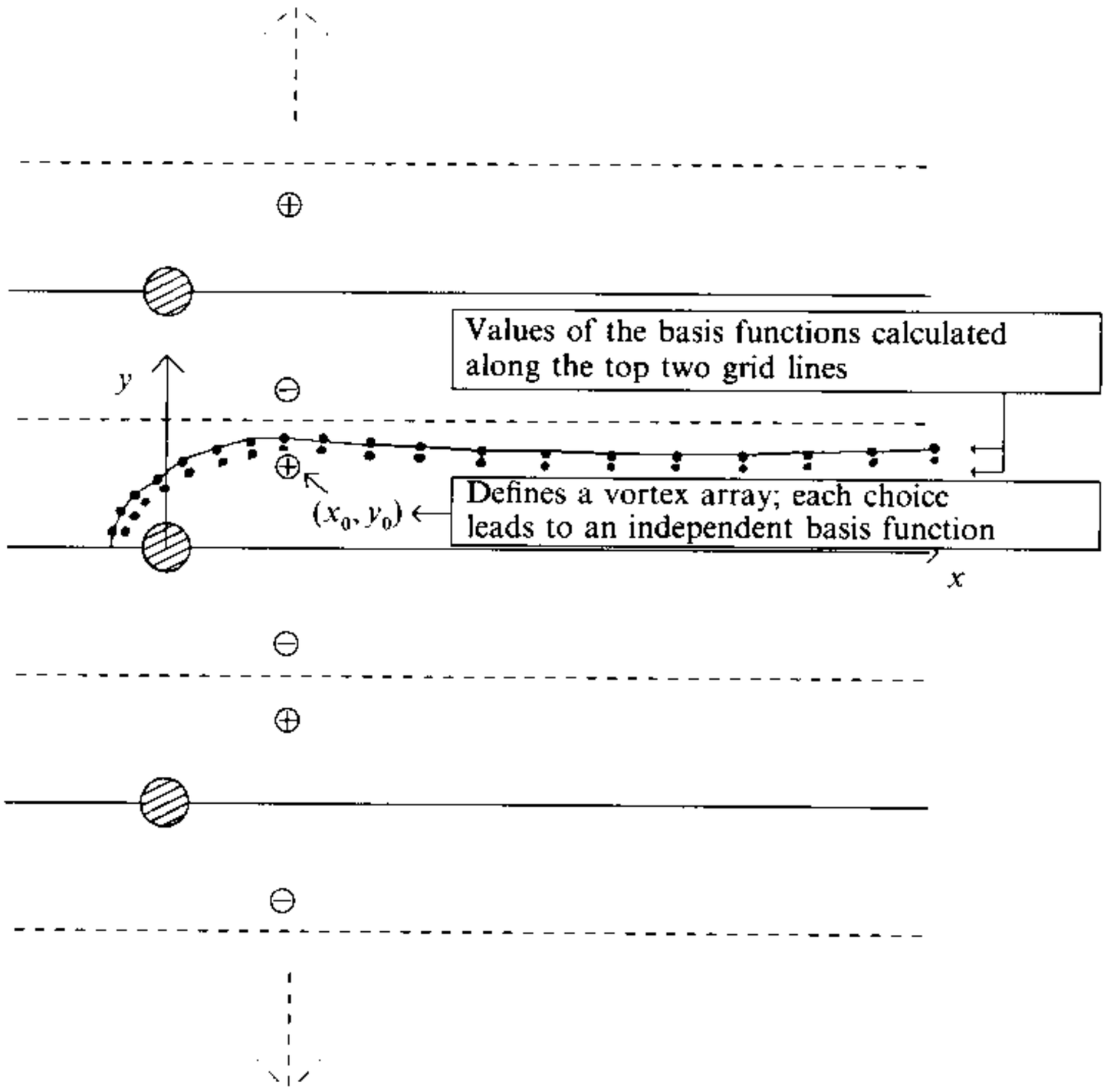

FIGURE 4. Generation of the top boundary condition for the wide code.

use of (5) and (6) to obtain the Z-variable of the narrow separation case. The reason for working with $\psi = \Psi - \Psi_{\text{pot}}$ rather than with Ψ is that this difference is a smoother function than Ψ itself, particularly near the top of the stretched grids. The truncation errors from finite differencing become smaller.

The boundary conditions along the left edge in the narrow code and the top edge in the wide code are implemented as described in Fornberg (1988). The required linearly independent sets of basis solutions are obtained by considering arrays of vortices, as indicated in figure 4 (in the case of the wide code). With point vortices of opposite signs located at (x_0, y_0) and $(x_0, -y_0)$ and periodically repeated every W units vertically, the stream function at an arbitrary position (x, y) becomes

$$\psi(x,y) = \frac{1}{4\pi} \ln \left\{ \frac{\cosh\left[2\pi(x-x_0)/W\right] - \cos\left[2\pi(y-y_0)/W\right]}{\cosh\left[2\pi(x-x_0)/W\right] - \cos\left[2\pi(y+y_0)/W\right]} \right\}. \tag{10}$$

All these basis solutions satisfy (3) for $\omega = 0$ and

$$\psi(x, kW/2) \equiv 0, \quad k = 0, \pm 1, \pm 2, \pm 3, \ldots. \tag{11}$$

They can therefore be used to impose the desired vertical W-periodicity.

Partly because of the relatively small extent of the downstream (outflow) boundary, the conditions imposed there proved not critical. The condition $\partial\omega/\partial\xi = 0$ (implemented over two adjacent grid points) serves the additional purpose of eliminating mesh size oscillations which otherwise may arise when centred approximations are used in convection–diffusion problems. As a second outflow condition, $\partial^2\Psi/\partial\xi^2 = 0$ was imposed (where Ψ is the 'full' stream function; not the perturbation ψ from potential flow).

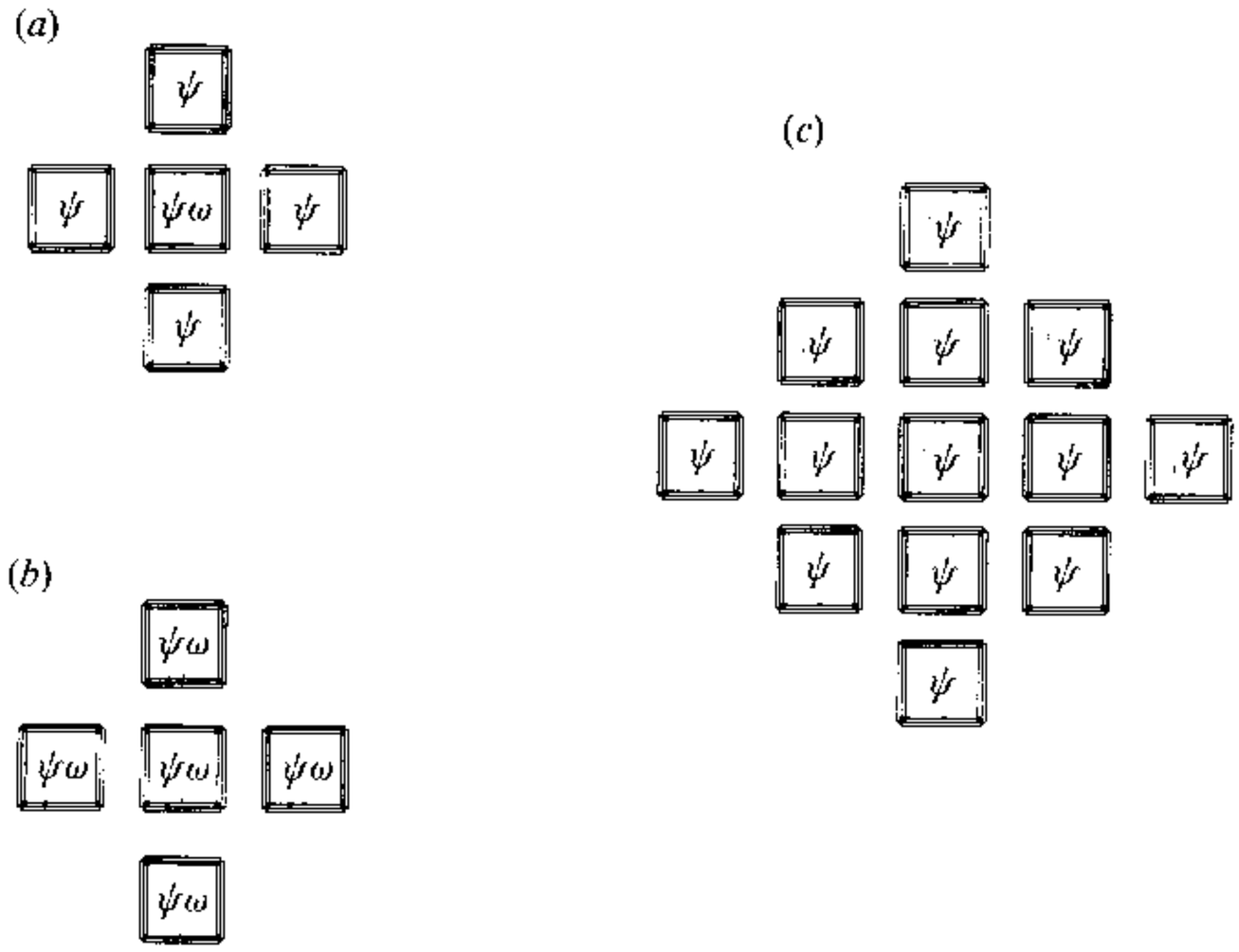

FIGURE 5. Stencils for the finite-difference approximations of the Navier–Stokes equations. (*a*) Five-point stencil corresponding to equation (3); (*b*) five-point stencil corresponding to (4); (*c*) 13-point stencil corresponding to (3) and (4) with ω eliminated.

For both codes, the G-plane grids consist of M columns (numbered 1 to M, left to right) and N rows (numbered 1 to N, bottom to top). On these grids, the stretched versions of (3) and (4), approximated by second-order finite differences, give rise to five-point stencils, as illustrated in figure 5(*a*, *b*) (showing at which point each unknown is present). Since ω appears explicitly, at one position only, in (3) (figure 5*a*), we substitute this expression for ω into the difference formula corresponding to (4) to obtain the (nonlinear) 13-point formula for ψ as indicated in figure 5(*c*).

Because of the extent of this 13-point stencil, two rows/columns of boundary conditions must surround the domain where we wish to use it. The details for these boundary conditions differ somewhat between the two codes:

Narrow code The unknown perturbation stream function ψ has to be calculated in rows 2 to $N-1$ and columns 1 to M (cf. figure 6*a*; for convenience of description, 'fictious' rows 0 and $N+1$ are added to the domain). In the different edge areas, the following boundary conditions are used:

(1) $\psi_{\text{row } N+1} = -\psi_{\text{row } N-1}$

(2) $\psi = 0$

(3) Asymptotic b.c. from basis functions as described above

(4) $\omega = 0$ (expressed in ψ)

(5) $\dfrac{\partial \omega}{\partial \xi} = 0$ (expressed in ψ)

(6) $\dfrac{\partial^2 \Psi}{\partial \xi^2} = 0$ (expressed in ψ)

(7) $\psi = 0$

(8) $\psi_{\text{row } 0} = -\psi_{\text{row } 2}$

(9) $\psi_{\text{row } 0} = \psi_{\text{row } 2}$

(10) $\psi_{\text{row } 0} = -\psi_{\text{row } 2}$.

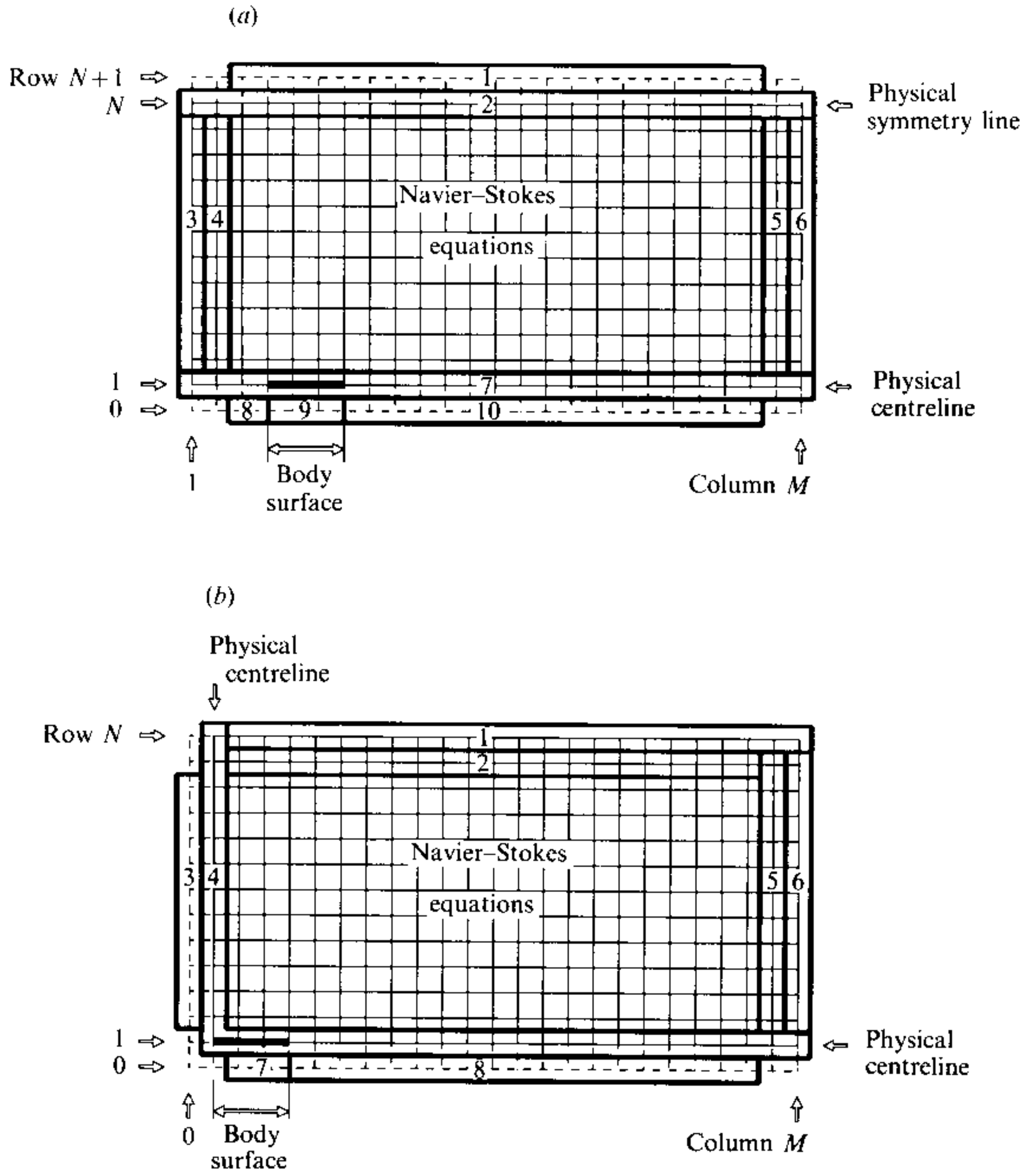

FIGURE 6. Implementation of the boundary conditions (in the G-planes). (a) Narrow code, (b) wide code.

Wide code The perturbation stream function ψ is unknown in rows 2 to N, columns 2 to M (cf. figure 6b; 'fictious' column 0 and row 0 are added). The following boundary conditions are used:

(1) Asymptotic b.c. from basis functions as described above

(2) $\omega = 0$ (expressed in ψ)

(3) $\psi_{\text{col}\,0} = -\psi_{\text{col}\,2}$

(4) $\psi = 0$

(5) $\dfrac{\partial \omega}{\partial \xi} = 0$ (expressed in ψ)

(6) $\dfrac{\partial^2 \Psi}{\partial \xi^2} = 0$ (expressed in ψ)

(7) $\psi_{\text{row}\,0} = \psi_{\text{row}\,2}$

(8) $\psi_{\text{row}\,0} = -\psi_{\text{row}\,2}$.

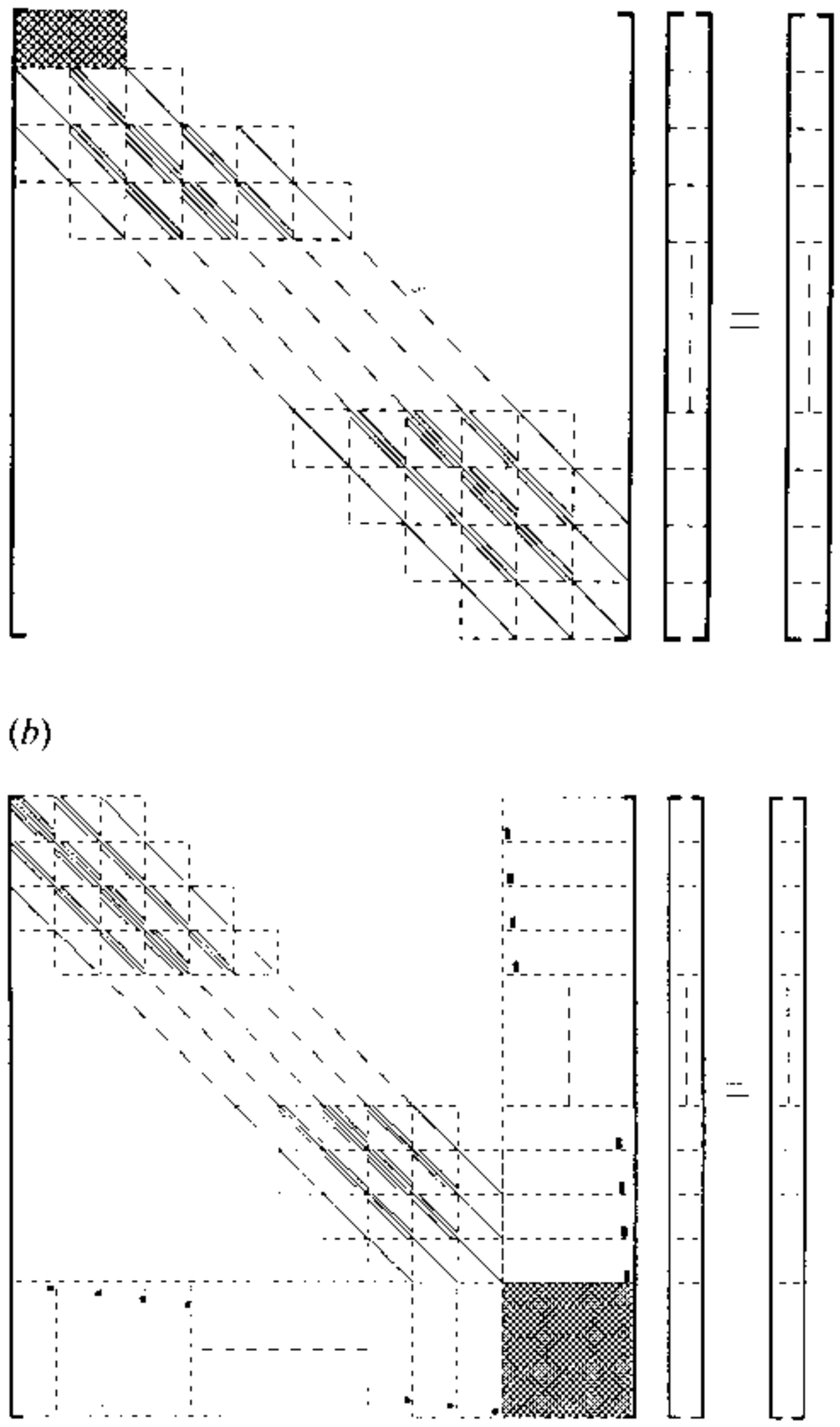

FIGURE 7. Structures of the linear systems to be solved using Newton's method. (*a*) Narrow code. (*b*) wide code.

5. Computational considerations

In the case of the narrow code, the most convenient ordering of the unknowns is by columns, from left to right. The coefficient matrix then takes the form shown in figure 7(*a*). Each of the minor blocks are of size $(N-2)\times(N-2)$; the system has M block rows. Pivoted Gaussian elimination can make full use of the zeros outside the outermost diagonals, but not the zeros between them. The solution of each system (bandwidth $4\times N-7$, $M\times(N-2)$ equations) involves approximately $16MN^3$ arithmetic operations. In the case of $M=937$, $N=181$, this takes about 12.8 min on the Cray X-MP/14se at Exxon Corporate Research. This corresponds to a sustained speed of about 115 Mflops (million floating operations per second, in 64-bit precision).

In the case of the wide code, the asymptotic top boundary condition leads to a more complex structure of the corresponding linear systems. With the unknowns ordered in columns 2 to M, elements 2 to $N-1$ followed by row N, columns 2 to M, it becomes as shown in figure 7(*b*). The small blocks are of size $(N-2)\times(N-2)$, the large one (in the bottom right corner) is $(M-1)\times(M-1)$. For each system there are, to leading order, $16MN^3+12M^2N^2$ operations (with an $M=701$, $N=121$ system requiring about 15.3 min, again corresponding to about 115 Mflops).

In both cases, the use of temporary disk storage during the Gaussian eliminations

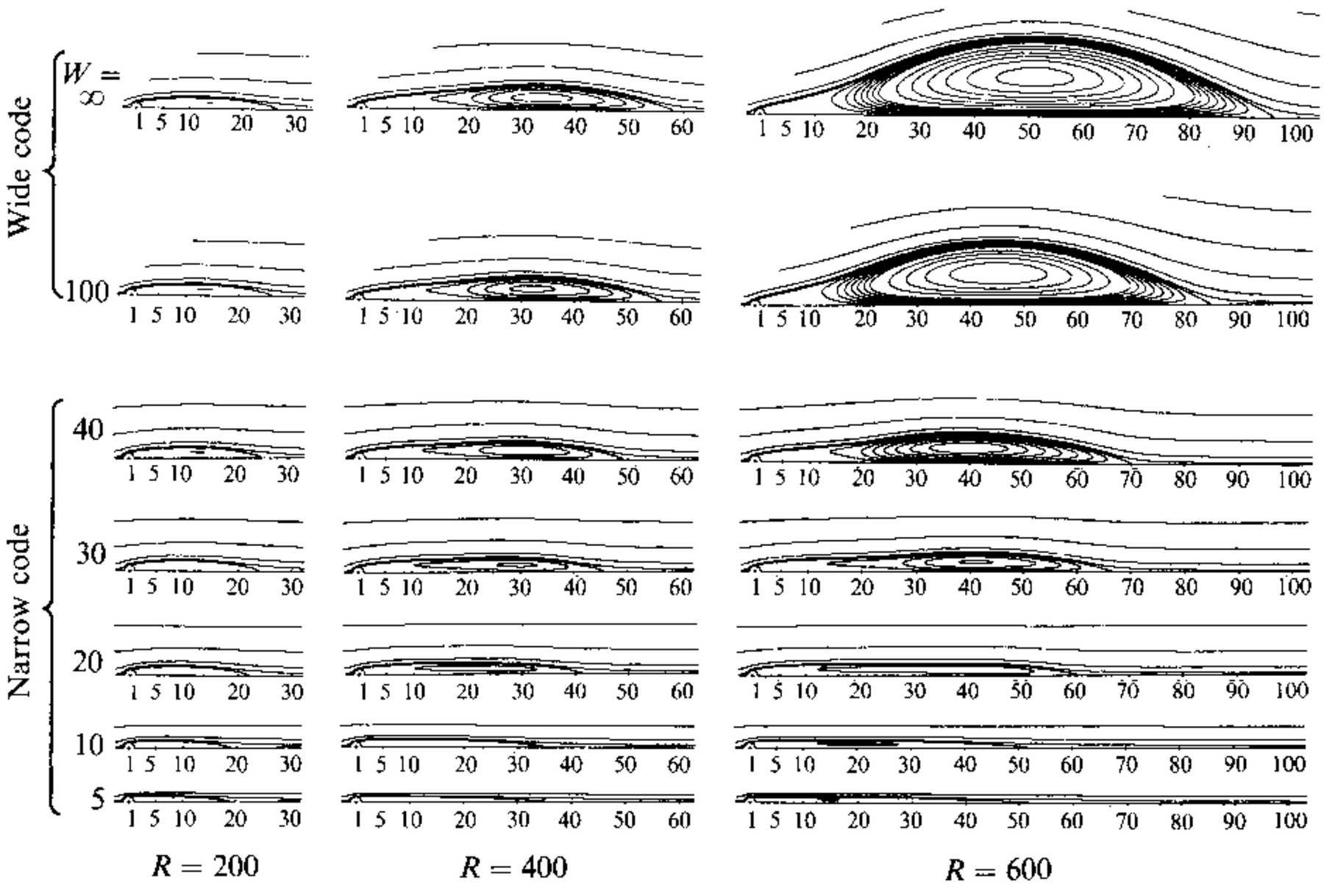

FIGURE 8. Streamlines for different values of R up to 600 and W up to ∞. Contour values: $|\{16, 9, 4, 1\}, \{0.2, 0, -0.2, \cdots -1.4\}, \{-2.0. -2.5, -3.0, \cdots\}|$.

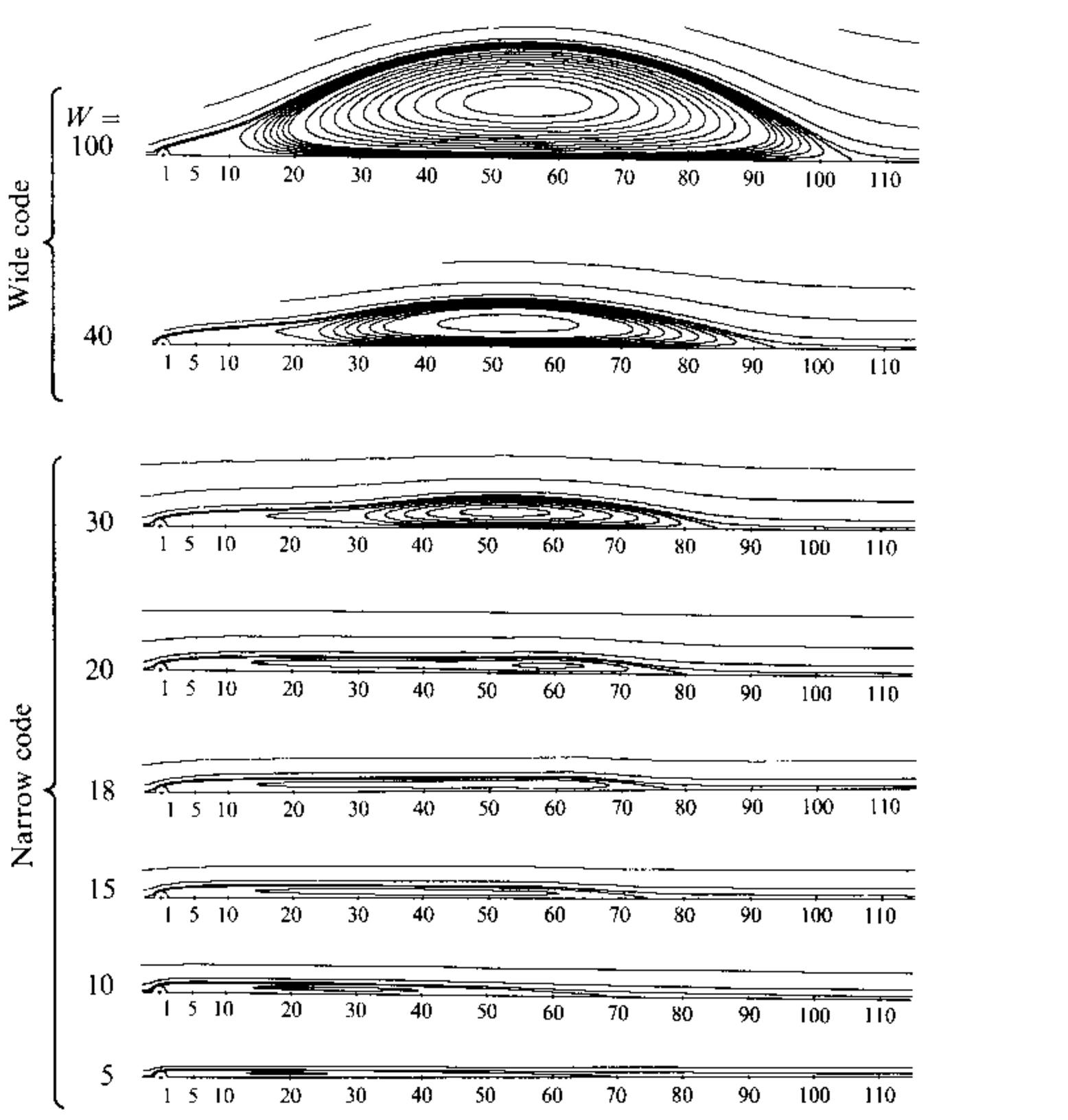

FIGURE 9. Streamlines for $R = 800$ and W up to 100.

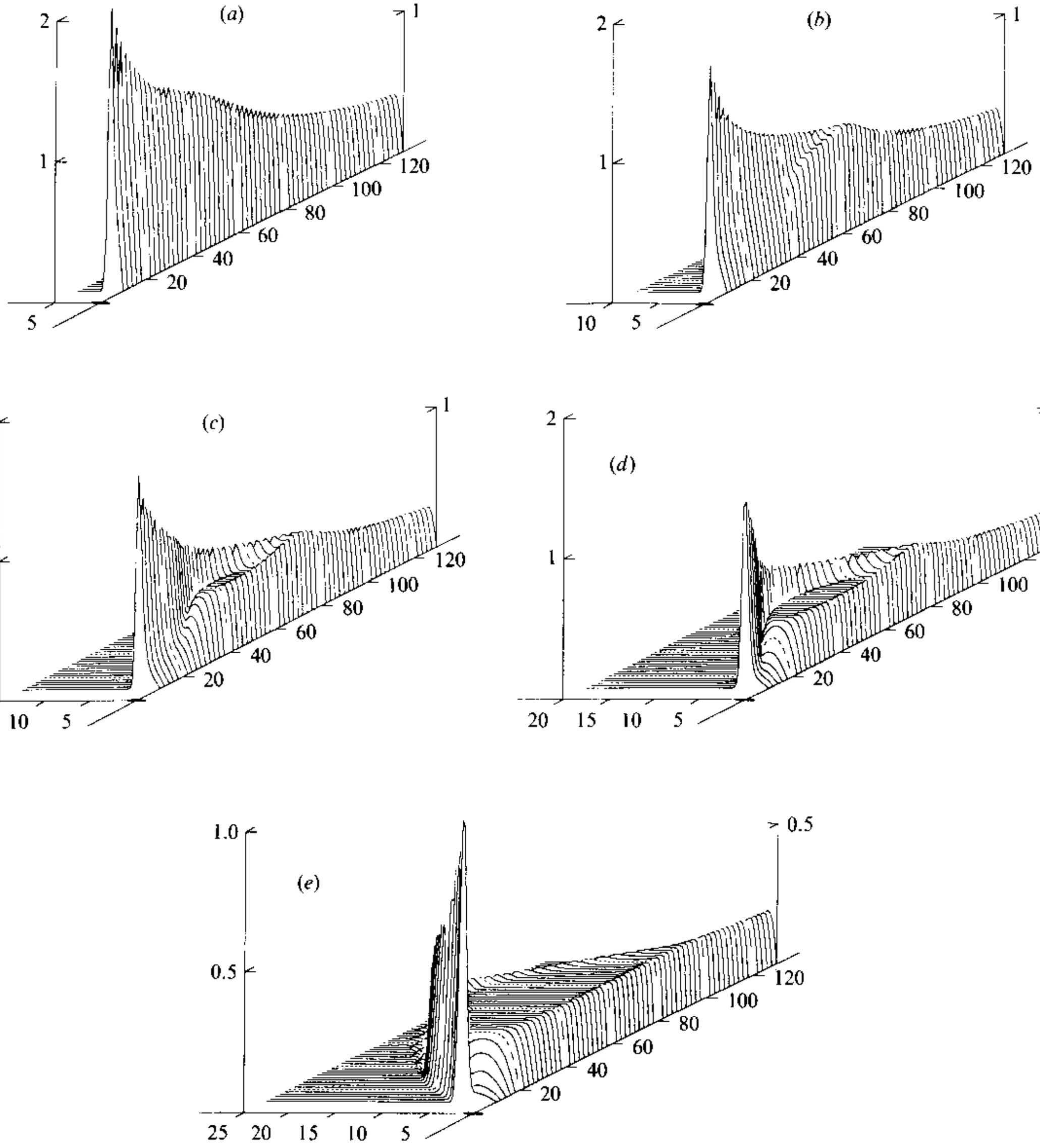

FIGURE 10. Vorticity fields at $R = 700$ for (*a*) $W = 10$, (*b*) 20 and (*c*) 30, (*d*) 40, (*e*) 100, (*f*) ∞.

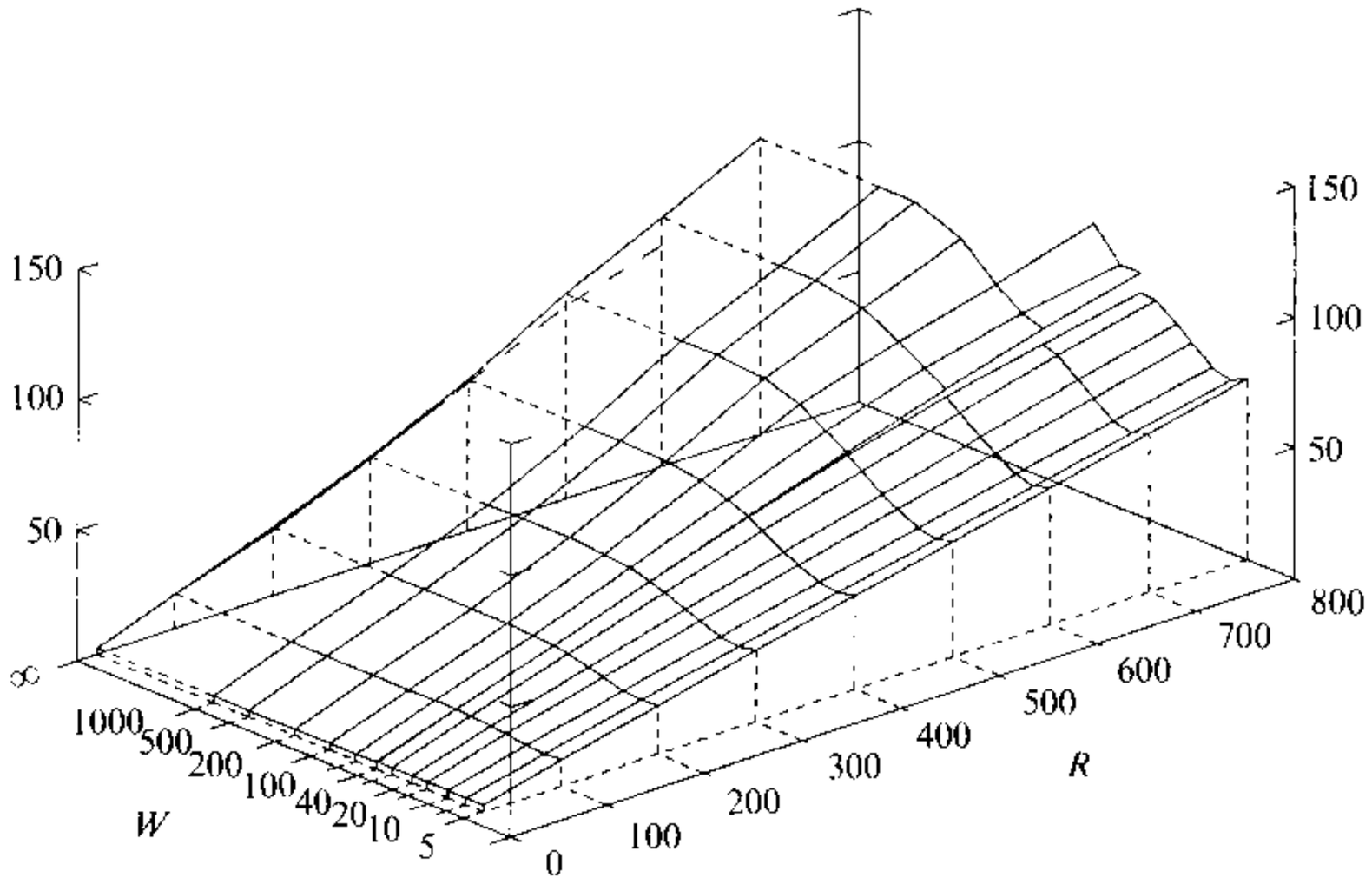

FIGURE 11. Lengths of the recirculation regions (measured from the centres of the cylinders).

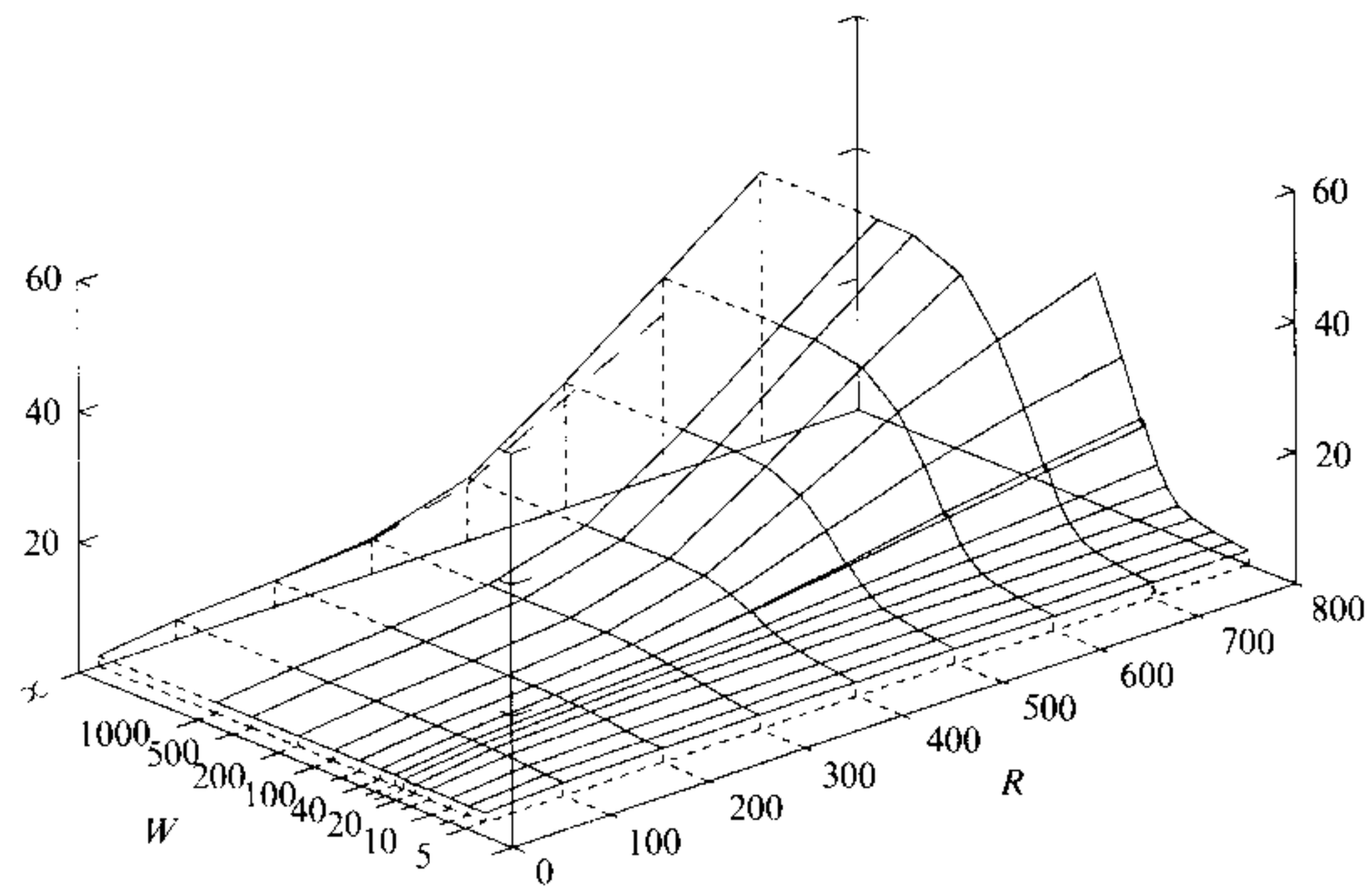

FIGURE 12. Widths of the recirculation regions (measured across both halves).

(of approximately 120 Mwords) allowed the codes to be run in less than 2 Mwords of main memory. By calculating the entries in the linear systems first when they were needed in the elimination and by operating double I/O-channels in parallel with the numerical calculations, the computations were CPU- (rather than I/O-) bound.

Typically four to five iterations were needed in each case for convergence to near-machine accuracy. Continuation between cases were performed by simple stepping in R or W.

6. Results

Figure 8 shows how the flow fields vary with W and R (up to 600). Figure 9 gives similar results for $R = 800$ and displays in particular the process by which long and

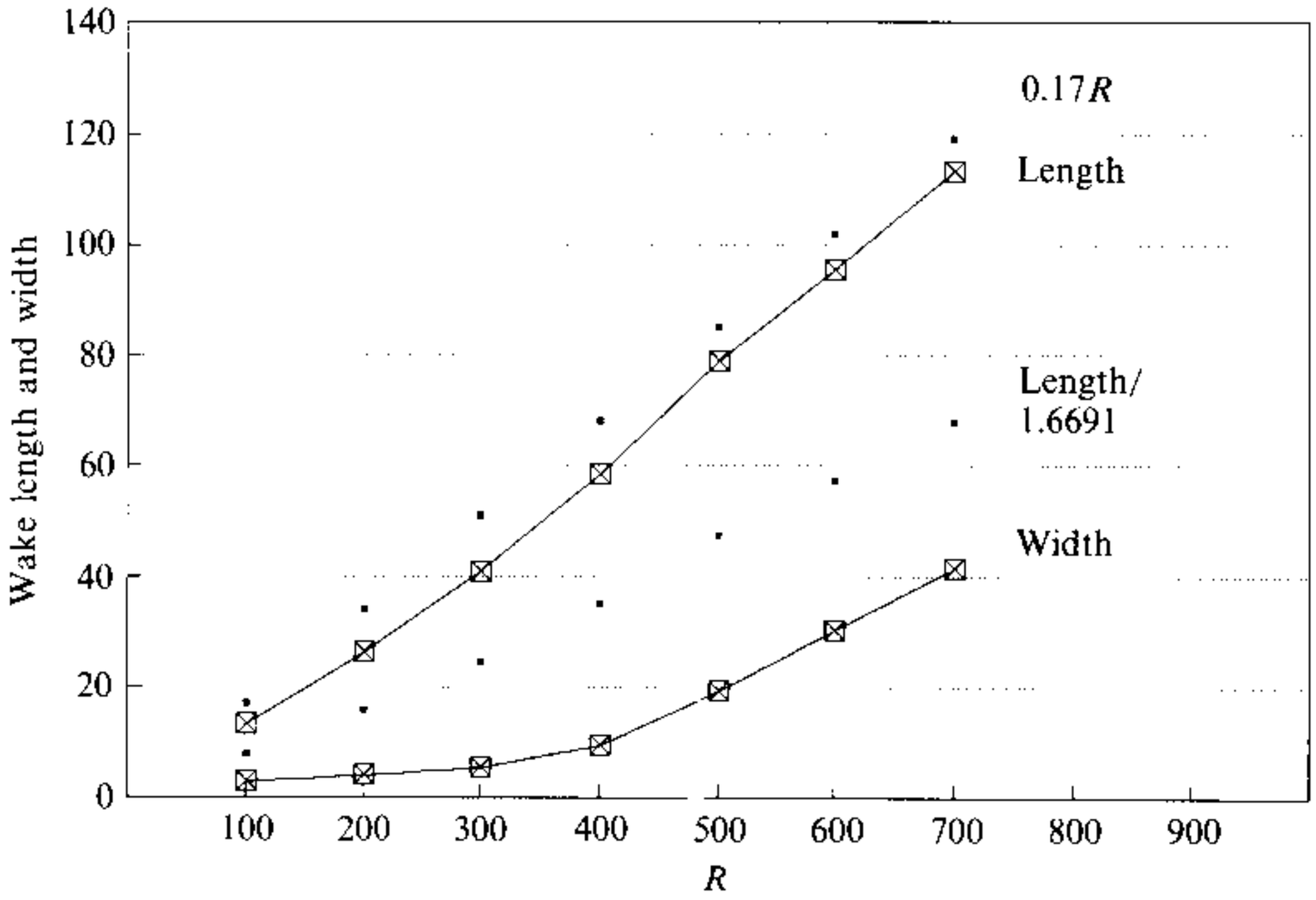

FIGURE 13. Lengths and widths of the recirculation regions for $W = \infty$.

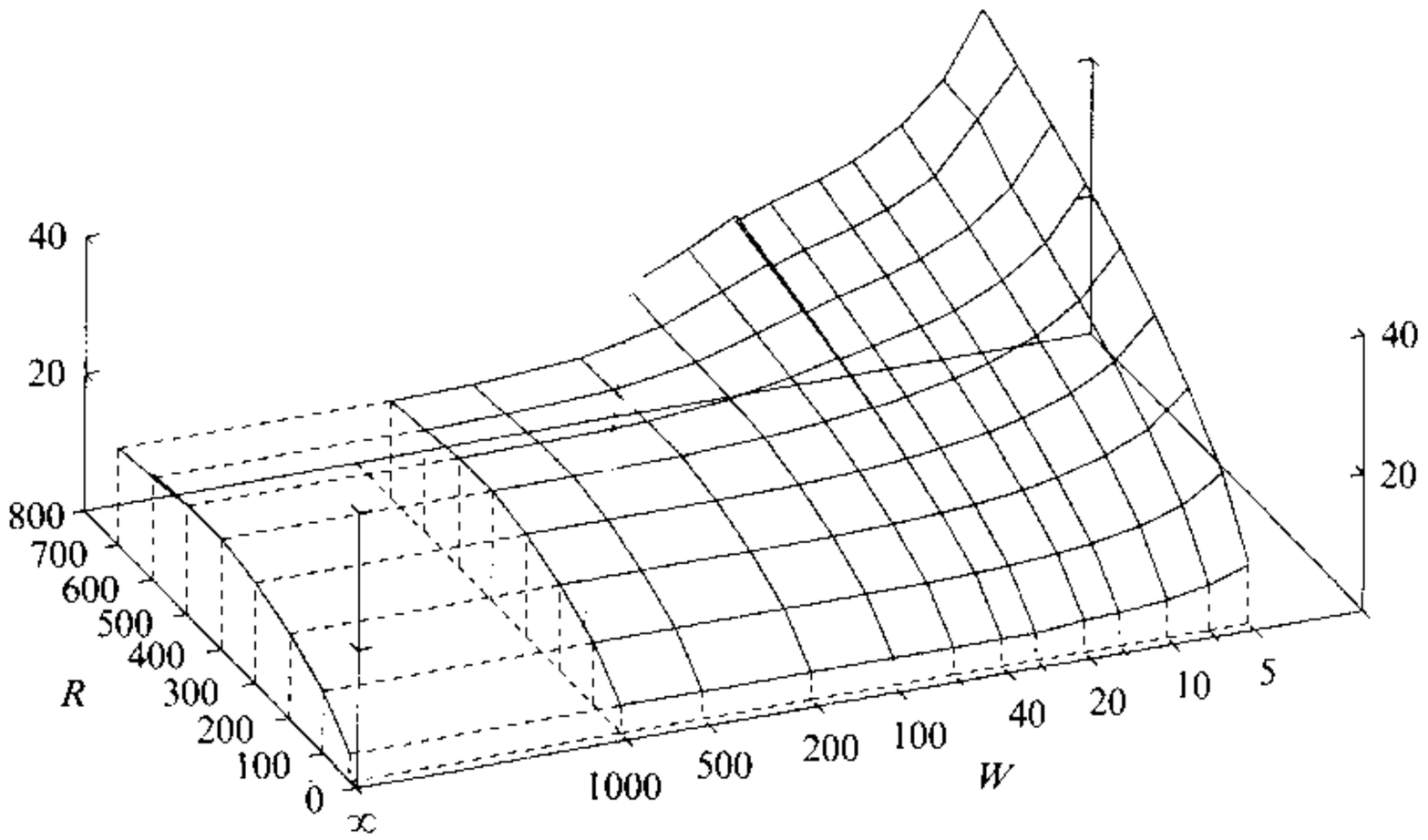

FIGURE 14. Maximal vorticity (in magnitude) on the cylinder surfaces.

slender wakes for $W < W_{\text{crit}}$ transform into wide (but still long) wakes as W is further increased, a 'bulge' starting to appear near the end of the recirculation region, but soon expanding to dominate the wake. Following $W = 20$ for $R = 200$, 400, 600 and 800 through figures 8 and 9 suggests a pattern for how the wake evolves for a fixed $W > W_{\text{crit}}$ when R is increasing. The 'bulge', which appears at the end of the wake, reaches a maximum size allowed by W and is then pushed further and further downstream.

Figure 10(*a f*) displays the structure of the vorticity fields at $R = 700$ and $W = 10$, 20, 30, 40, 100 and ∞ respectively (with the sign reversed; the vorticity is negative throughout the displayed areas). Note that the scales on the x- and y-axes differ, as can be seen from the labels as well as from the distorted shape of the circular cylinder at the origin. The first four parts (figure 10*a–d*) extend in the y-direction up

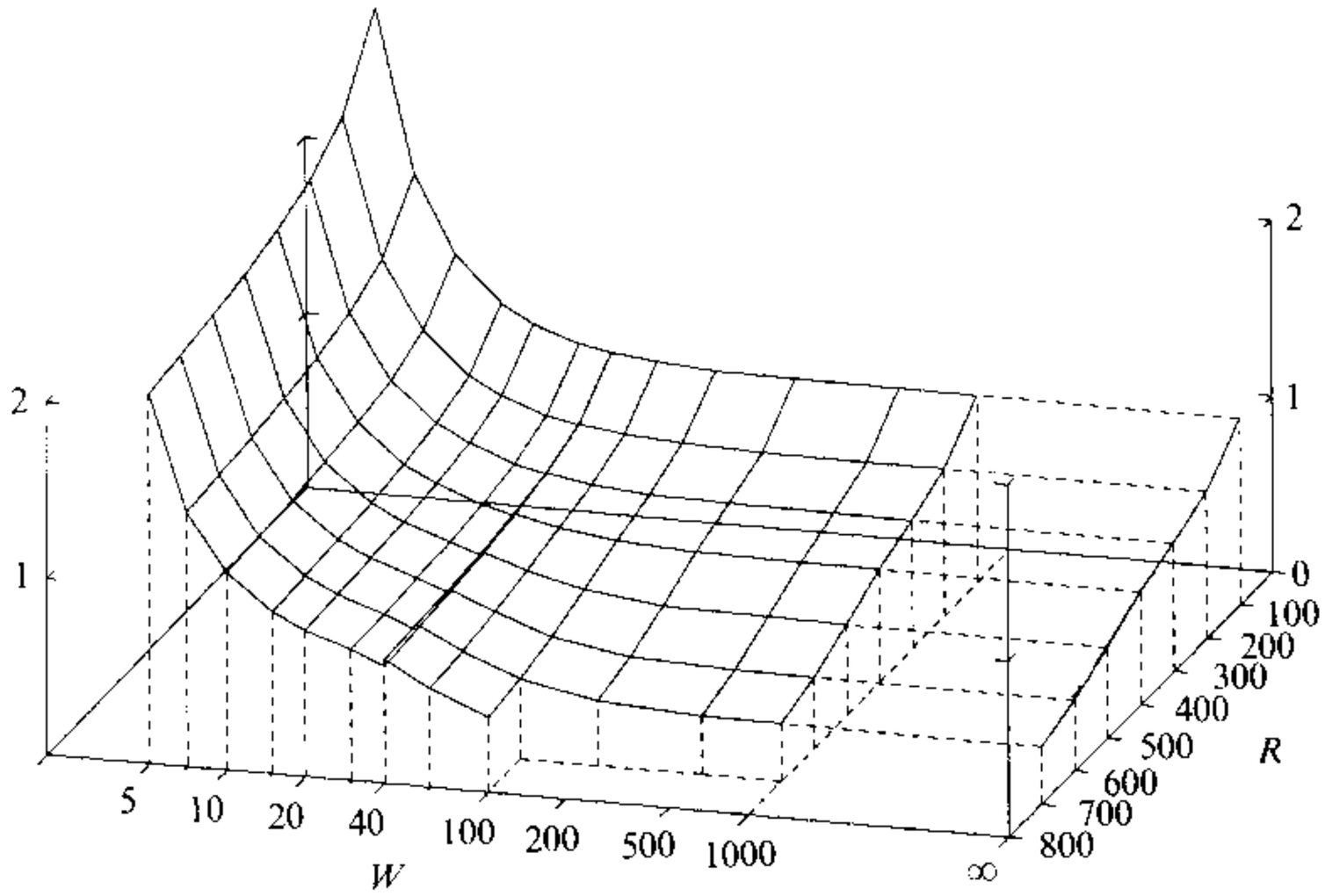

FIGURE 15. Drag coefficients C_D.

to the physical line of symmetry (at $y = \frac{1}{2}W$), the last two (figures 10*e*, *f*) do not, and also have a different vertical scale. Figures similar to these, but with W fixed ($= \infty$) and R increasing (up to 600) were presented in Fornberg (1985).

Figures 11 and 12 show the lengths and the widths of the recirculation regions, measured from the centre of the cylinder and across the full wake respectively. The results for $R \leqslant 600$, $W = \infty$ from Fornberg (1985) are included for comparison in figures 11 and 12 as well as in figures 14 and 15 described later (marked by long dashes). It is only in these two cases (figures 11 and 12) that there are any noticeable differences between the two studies. Figure 13 illustrates the near-linear trends for lengths and widths for large R in the case of a singular cylinder ($W = \infty$). The upper set of dotted data satisfy the relation $L = 0.17R$, proposed by Smith (1979) as an approximation to the wake length. The slope of the lower set of dotted data (length/1.6691) is indistinguishable from that of the wake width. This relationship between these two trends supports the idea that the wakes, at the highest Reynolds numbers considered here, can be described as perturbations of the self-propagating Euler solutions (as described by Sadovskii 1971) in their limit of vanishing vortex sheet strengths. In this limit the aspect ratio, length/width, is minimal, approximately 1.6691 according to Wu, Overman & Zabusky (1984).

Figure 14 displays the maximum vorticity values (in magnitude) on the body surface. As in Fornberg (1985), the peak vorticity is seen to decrease for increasing R at high W (owing to the influence of the rapidly widening wake on the incoming flow).

The drag coefficients C_D were calculated from integrals along the cylinder surfaces, corresponding to the relation (in polar coordinates):

$$C_D = \frac{4}{R}\int_0^{\pi} (\omega_r - \omega)\sin\theta \, \mathrm{d}\theta. \tag{12}$$

Results for C_D are shown in figure 15.

Table 4 gives numerical values for the data displayed graphically in figures 11, 12, 14 and 15.

Length of recirculation region

W	$R = 100$	200	300	400	500	600	700	800
5	10.0	18.6	27.1	35.5	43.9	52.3	60.7	69.1
10	10.3	18.8	27.1	35.3	43.5	51.7	59.9	68.1
20	11.9	22.0	31.8	41.5	51.1	60.6	70.0	79.3
40	12.9	24.8	36.9	49.2	61.0	71.8	81.3	89.5
100	13.2	26.1	40.1	56.1	72.8	84.5	94.0	105
1000	13.2	26.2	40.8	58.2	78.9	95.4	113	—
∞	13.2	26.2	40.8	58.2	78.9	95.4	113	—

Width of recirculation region

W	$R = 100$	200	300	400	500	600	700	800
5	1.97	2.09	2.14	2.17	2.19	2.20	2.21	2.22
10	2.37	2.67	2.80	2.87	2.92	2.95	2.97	2.99
20	2.71	3.37	3.76	3.98	4.10	4.26	4.51	4.75
40	2.82	3.82	4.77	6.37	8.63	11.1	13.4	14.7
100	2.88	3.98	5.40	9.02	16.4	24.1	30.0	35.1
1000	2.88	4.00	5.46	9.51	19.2	30.2	41.2	—
∞	2.88	4.00	5.46	9.51	19.2	30.2	41.2	—

Maximum vorticity on body surface

W	$R = 100$	200	300	400	500	600	700	800
5	17.8	25.1	30.7	35.4	39.6	43.4	46.8	50.0
10	12.2	17.4	21.4	24.7	27.7	30.4	32.8	35.1
20	10.3	14.5	17.8	20.6	23.1	25.3	27.4	29.3
40	9.5	13.1	16.0	18.4	20.5	22.4	24.2	25.8
100	9.2	12.6	15.0	16.7	17.4	17.6	18.0	18.6
1000	9.0	12.4	14.7	16.1	15.8	14.9	14.1	—
∞	9.0	12.4	14.7	16.1	15.8	14.9	14.1	—

Drag coefficient

W	$R = 100$	200	300	400	500	600	700	800
5	2.974	2.543	2.374	2.278	2.214	2.168	2.131	2.100
10	1.608	1.363	1.269	1.216	1.181	1.156	1.135	1.119
20	1.248	1.028	0.948	0.906	0.879	0.859	0.844	0.831
40	1.125	0.900	0.813	0.767	0.737	0.714	0.697	0.684
100	1.072	0.847	0.747	0.672	0.581	0.503	0.453	0.424
1000	1.060	0.831	0.727	0.639	0.514	0.404	0.329	—
∞	1.060	0.831	0.726	0.639	0.514	0.403	0.328	—

TABLE 4. Some different flow quantities as functions of R and W: numerical values for the data displayed in figures 11, 12 14 and 15

7. Discussion of numerical errors

Figure 16 illustrates the domains in the (R, W)-plane where the two codes were employed. The cylinder separation $W = 40$ is particularly difficult in both cases. With the narrow code, the vertical extent is then large compared to the finest scales that have to be resolved. Regarding the wide code, the top boundary implementation becomes inaccurate if this boundary overlaps with its image belonging to the cylinder above. With the grid in figure 3(*a*) (extending vertically to 22.6), W has to exceed 45.2. (To use the code all the way down to $W = 40$ required a few top grid lines to be removed, leaving only minimal clearance between the top of the wake and the top

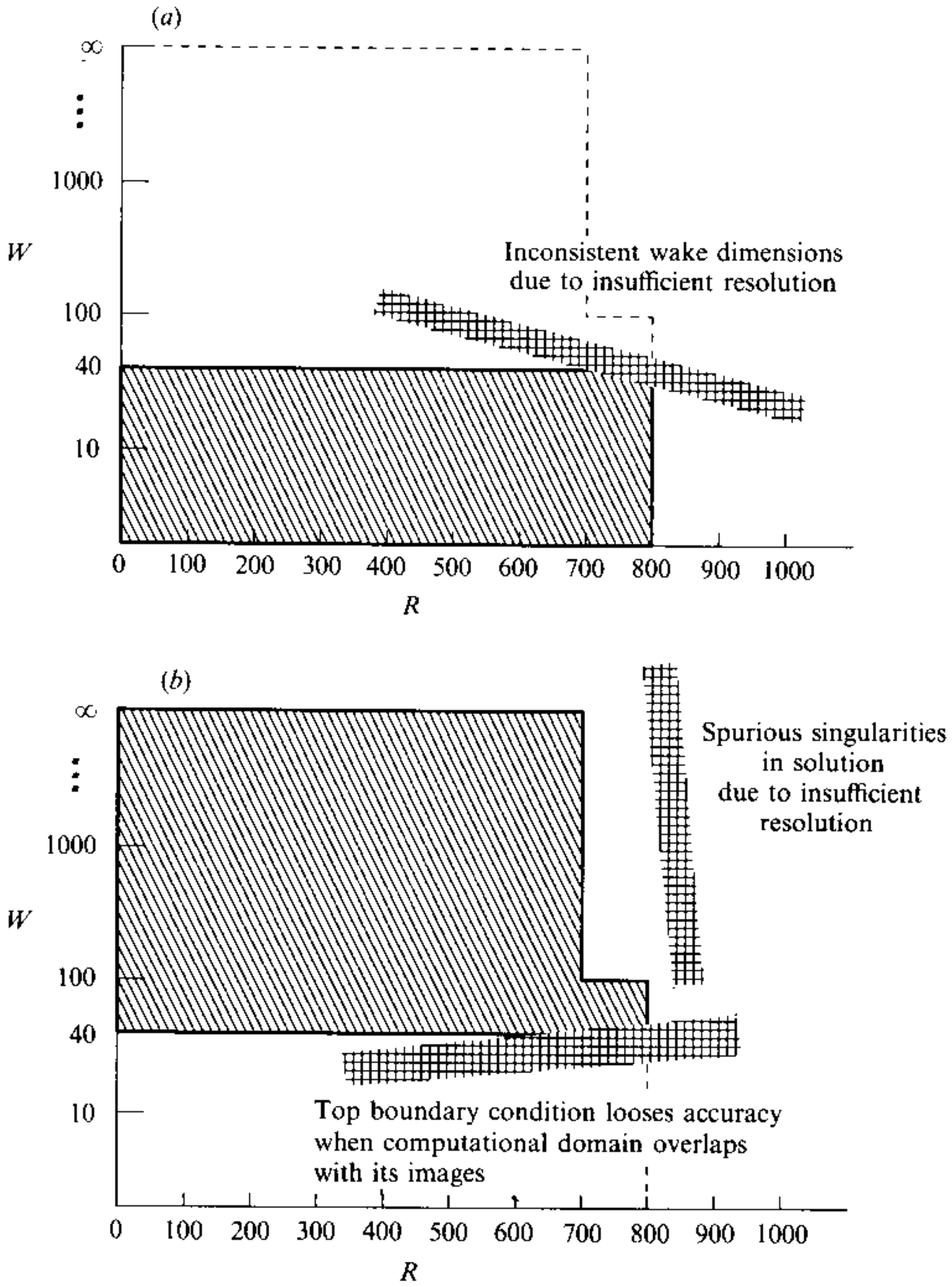

FIGURE 16. Restrictions on the domains in the (R, W)-plane where the two codes maintain satisfactory accuracies. (*a*) Narrow code, (*b*) wide code.

boundary). The cross-hatched rectangular strips in figure 16 suggest the approximate location of the different 'barriers' limiting the present calculations from further extensions in W and R (with the present grid densities).

With the possible exception of the wake length, the variable most sensitive to small errors, there is good agreement between the two codes around $W = 40$, as seen in figures 11, 12, 14 and 15. A succession of coarser grids was used to verify that convergence under mesh refinement always occurred at the rates, asymptotically to be expected from second-order-accurate schemes.

With both codes, insufficient grid resolution invariably gave rise to spurious Prandtl–Batchelor wakes of relatively small size. This might support the idea that such wakes indeed do arise for slightly perturbed problems (this would be consistent with such solutions being reported by Milos *et al.* 1987). Since the wakes for large values of R and W appear to be quite sensitive to even small changes in the velocity profile near the bodies, further calculations with different body shapes would be desirable.

REFERENCES

Batchelor, G. K. 1956 A proposal concerning laminar wakes behind bluff bodies at large Reynolds number. *J. Fluid Mech.* **1**. 388.

Fornberg, B. 1981*a* Numerical differentiation of analytic functions. *ACM Trans. Math. Software* **7**, 512.

Fornberg, B. 1981*b* Algorithm 579 CPSC: Complex power series coefficients. *ACM Trans. Math. Software*, **7**, 542.

Fornberg, B. 1985 Steady flow past a circular cylinder up to Reynolds number 600. *J. Comput. Phys.* **61**, 297.

Fornberg, B. 1988 Steady viscous flow past a sphere at high Reynolds numbers. *J. Fluid Mech.* **190**, 471.

Ingham, D. B., Tang, T. & Morton, B. R. 1990 Steady two-dimensional flow through a row of normal flat plates. *J. Fluid Mech.* **210**, 281.

Milos, F. S. & Acrivos, A. 1986 Steady flow past sudden expansions at large Reynolds number. Part I: Boundary layer solutions. *Phys. Fluids* **29**. 1353.

Milos, F. S., Acrivos, A. & Kim, J. 1987 Steady flow past sudden expansions at large Reynolds number. II. Navier–Stokes solutions for the cascade expansion. *Phys. Fluids* **30**, 7.

Sadovskii, V. S. 1971 Vortex regions in a potential stream with a jump of Bernoulli's constant at the boundary. *Appl. Math. Mech.* **35**. 729.

Smith, F. T. 1979 Laminar flow of an incompressible fluid past a bluff body: the separation, reattachment, eddy properties and drag. *J. Fluid Mech.* **92**, 171.

Smith. F. F. 1985 On large-scale eddy closure. *J. Math. Phys. Sci.* **19**. 1.

Wu, H. M., Overman, E. A. & Zabusky, N. J. 1984 Steady state solutions of the Euler equations in two dimensions: Rotating and translating V-states with limiting cases. 1. Numerical algorithms and results. *J. Comput. Phys.* **53**, 42.